Optica Applicata, Vol. LIII, No. 2, 2023
DOI: 10.37190/oa230203

An extrinsic Fabry–Pérot interference fiber sensor for ultrasonic detection of partial discharge

Ximin Zhang[1], Sen Qian[1], Huixin Liu[2], Chuan Chen[1],
Chuanlu Deng[3], Chengyong Hu[3], Yi Huang[3,*]

[1]State Grid Smart Grid Research Institute Co., Ltd, Beijing 102211, China

[2]Electric Power Research Institute, SGCC, Fuzhou 350007, China

[3]Key Laboratory of Specialty Fiber Optics and Optical Access Networks,
Joint International Research Laboratory of Specialty Fiber Optics and Advanced Communication,
Shanghai University, Shanghai 200444, China

[*]Corresponding author: huangyi1008@shu.edu.cn

An ultrasonic sensor based on extrinsic Fabry–Pérot interference (EFPI) has been designed and demonstrated to detect the ultrasonic wave signal. The sensitivity and natural frequency of fiber Fabry–Pérot (F-P) sensor with different structure parameter have been simulated by COMSOL. The simulation results illustrate that the sensitivity is up to 1.737 nm/kPa and the natural frequency is 2.1 MHz, when the silica diaphragm thickness is 2 μm, the radius is 90 μm, and the cavity length is 18 μm. The most suitable parameters have been selected and the F-P sensor has been fabricated. When the ultrasonic signals with the frequencies of 40 kHz and 1.2 MHz are respectively applied to the sensor, the frequencies detected by the EFPI ultrasonic sensor are 39 kHz and 1.21 MHz based on a partial discharge detection experiment for the designed demodulation system. The experimental results show that the sensor can accurately detect ultrasonic signals. As an excellent platform for ultrasonic signal sensing, this EFPI ultrasonic sensing system has great potential applications in partial discharge detection field.

Keywords: extrinsic Fabry–Pérot interference, fiber sensor, partial discharge, sensitivity, frequency.

1. Introduction

Gas insulated switchgear (GIS) is the core power transmission and transformation equipment in the power system, and its operational reliability is very important to the safety and stability of the power grid [1–3]. According to the statistical results of related GIS faults, GIS insulation faults account for a large proportion [4], which brings hidden dangers to the safe and stable operation of the power grid. The ability to accurately predict and locate GIS insulation faults is an important prerequisite for safe operation [5]. When a GIS insulation fault occurs, one of the notable features is partial discharge (PD), and the phenomena such as light, ultrasonic waves, and electromagnetic radiation will be generated [6, 7]. These reactions can be used to detect the PD signal.

The more commonly used detection methods of the PD signal are pulse current method [8,9], ultra-high frequency detection method [10–15], ultrasonic detection method [16] and optical detection method [17–21]. Electric sensing method and ultra-high frequency method are susceptible to electromagnetic interference, but they are not suitable for PD sensing in a strong electromagnetic environment. Although the ultra-high frequency method and ultrasonic sensing method can resist electromagnetic interference to a certain extent, its detection accuracy is not enough. Compared with traditional electrical sensors, optical fiber sensors have the advantages of small size, light weight, high sensitivity, high frequency response, and anti-electromagnetic interference, therefore it is more suitable for the PD detection. Combining optical fiber sensing technology with ultrasonic detection method to detect PD signals is a very good detection method. In 2000, a fiber coil acoustic sensor proposed by ZHAO *et al.* can detect sound waves below 150 kHz [22]. In 2015, a PD ultrasonic sensor based on fiber Bragg grating is reported by ZHENG *et al.*, and a high sensitivity of –79.503 dB at 108 kHz was obtained [17]. In 2019, an optical fiber acoustic emission sensor based on interference has been proposed by MA *et al*., and high amplitude of the signal detected by this system can be achieved [23]. However, the structure of these PD ultrasonic detection system is very complicated. In 2020, LI proposed an EFPI ultrasonic sensor with two resonant frequencies which are 31 and 63 kHz [24], but these two frequencies are relatively low relative to the frequency of the detected signal.

In this study, an EFPI ultrasonic sensor with high frequency response (2.1 MHz) and small size has been designed and manufactured. First, the fiber Fabry–Pérot (F-P) sensor with different diaphragm structure parameters is simulated based on the COMSOL finite element simulation software. The relationship between the sensitivity and natural frequency with the structure parameters of the silica diaphragm have been investigated. Then in the experiment, the ultrasonic signals with the frequency of 40 kHz and 1.2 MHz are applied to the fiber F-P sensor, and the experimental results were consistent with the theoretical simulation. To verify the accuracy of the system, more professional tests were carried out at the Shanghai Institute of Metrology. An ultrasonic signal was applied to PZT and EFPI ultrasonic sensor simultaneously, and the frequency of the ultrasonic signal detected by the PZT and EFPI ultrasonic sensor are compared and analyzed.

2. Sensing theory and sensor design

Figure 1 shows a schematic diagram of the fiber F-P sensor. The entire fiber F-P sensor is composed of a silica diaphragm, a silica tube, a fiber tube, and a single-mode fiber (SMF). Light enters the F-P cavity from SMF, a part of the light is reflected back from the SMF end-face, another part is transmitted into the F-P cavity, then reflected back to the fiber core from the silica diaphragm. The entire light intensity I reflected to the SMF core can be written as [25]

$$I(\lambda, L) = \left[R_1 + R_2 - 2\sqrt{R_1 R_2}\cos\left(\frac{4\pi n_0 L}{\lambda}\right)\right] I_0(\lambda) \tag{1}$$

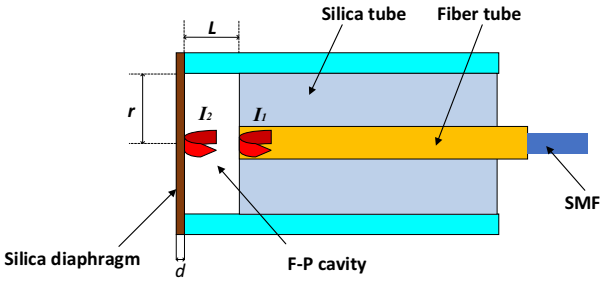

Fig. 1. Schematic diagram of fiber F-P sensor probe.

where R_1 and R_2 are the reflectivity of the SMF endface and the silica diaphragm, respectively. L is the length of F-P cavity, n_0 is the index of the F-P cavity, λ is wavelength, and $I_0(\lambda)$ is the intensity of the input light at different wavelength.

It can be seen from Eq. (1) that the intensity of the reflected light will be changed with the F-P cavity length. Therefore, when PD occurs, the ultrasonic signal generated by the PD will act on the silica diaphragm of the F-P, and the cavity length of the fiber F-P sensor will change, which causes the optical path difference of the two beams to change, and finally results in the intensity of the reflected light changes.

The sensitivity, center displacement and response frequency of the silica diaphragm determine the measurement range and accuracy of the sensor [1]. When the elastic deformation of the silica diaphragm is less than 20% of its thickness, its deformation is proportional to the pressure [26]. For the center point of the silica diaphragm, the sensitivity of its compression deformation can be expressed as [27]

$$\frac{y_{\max}}{P} = \frac{3(1-\mu^2)r^4}{16Ed^3} \tag{2}$$

where μ is Poisson's ratio, E is Young's modulus, r and d are radius and thickness of the silica diaphragm, respectively, $y_{\max}$ is the maximum displacement of the silica diaphragm, and P is the pressure. It can be seen from Eq. (2) that the displacement of the silica diaphragm is only related to the thickness and radius in the geometric parameters of the silica diaphragm, but has nothing to do with the F-P cavity length.

The natural frequency of circular diaphragm f_{00} can be expressed as [27]

$$f_{00} = \frac{k_{00}^2}{4}\sqrt{\frac{E}{3\rho(1-\mu^2)}}\frac{d}{r^2} \tag{3}$$

where k_{00} is the first order resonance constant of 3.196, ρ refers to the material density of the diaphragm. According to this Eq. (3), the length of the cavity has no effect on the natural frequency.

When the natural frequency of the silica diaphragm matches the frequency of the detection signal, the sensitivity of the fiber F-P sensor may reach the maximum. How-

ever, when the natural frequency of the diaphragm is less than the frequency of the detection signal, the diaphragm will not vibrate and the signal cannot be detected [1]. Thus, the natural frequency of the silica diaphragm used in the actual measurement must be larger than the frequency of the detected PD ultrasonic signal.

To obtain the best structure parameter of the silica diaphragm, numerical simulation based on COMSOL multiphysics simulation software has been performed, where the solid pressure as the sound pressure generated by ultrasonic wave act on the diaphragm. Considering the universality of silica and the same material as optical fiber, silica is used as the material of the fiber F-P sensor. First, the relationship between the thickness of silica diaphragm and the sensitivity and natural frequency is determined. When the silica diaphragm radius is 90 μm and the cavity length is 18 μm, the reflection spectra of the fiber F-P sensor with different pressure and silica diaphragm thickness have been illustrated in Figs. 2(a) and (b). The reflection spectra have a blue shift of central wavelength when the pressure increases. When the thickness of the silica diaphragm increases, the blue shift decreases. It is clear from Figs. 2(a) and (b) that the blue shift with the silica diaphragm thickness of 2 μm is greater than that with thickness of 5 μm. Generally, the greater blue shift, the greater sensitivity of the fiber FP sensor. As shown in Fig. 2(c), when the thickness of the silica diaphragm increases, the sensitivity decreases, but the natural frequency increases. Based on the simulation results above, the thickness of the silica diaphragm is chosen as 2 μm, which can obtain high sensitivity and ensure that the natural frequency meets the frequency requirements of measuring the ultrasonic signal.

The sensitivity and natural frequency with increase of the radius of silica diaphragm is also studied further. The silica diaphragm thickness is 2 μm, and the cavity length

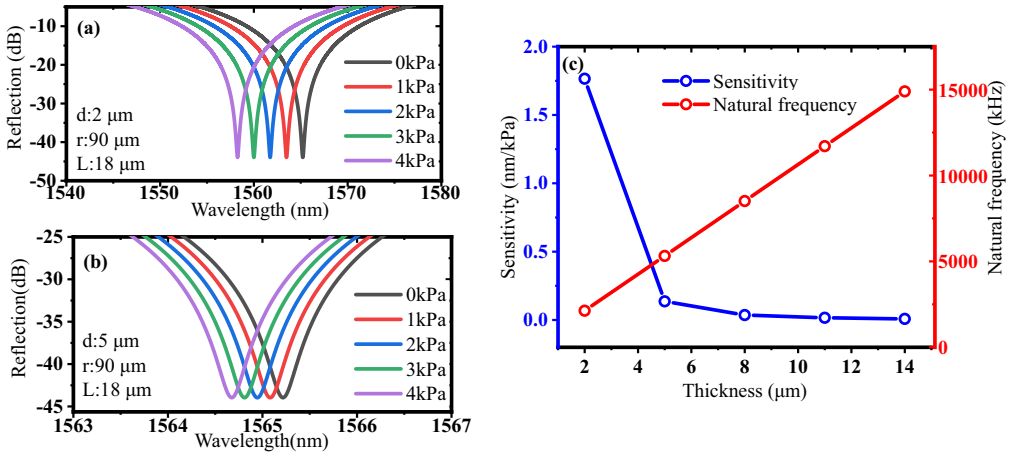

Fig. 2. Reflection spectra of the fiber F-P sensor under different pressure with the silica diaphragm thickness of (a) 2 μm, (b) 5 μm, and (c) the sensitivity and natural frequency with the silica thickness.

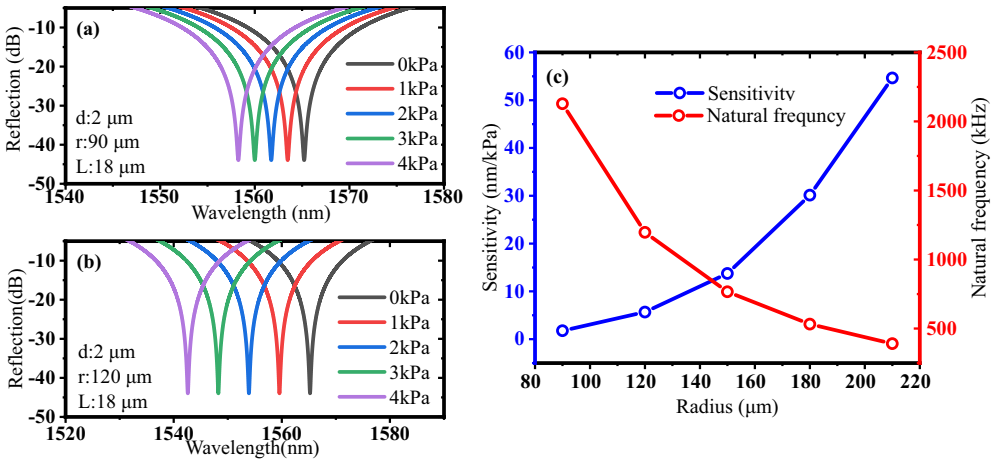

Fig. 3. Reflection spectra of the fiber F-P sensor under different pressure with the silica diaphragm radius of (a) 90 μm, (b) 120 μm, and (c) the sensitivity and natural frequency with the radius of silica diaphragm.

is 18 μm. Figures 3(a) and (b) show the reflection spectra of the fiber F-P sensor with different silica diaphragm radius under different pressure. It is indicated that the blue shift with the radius of 120 μm is greater than that with the radius of 90 μm. The relationship between sensitivity and silica diaphragm radius, and that between natural frequency and silica diaphragm radius are depicted in Fig. 3(c). It can be seen from Fig. 3(c) that the sensitivity increases and the natural frequency decreases with the increase of silica diaphragm radius. In order to balance the sensitivity and the detection range, the silica diaphragm radius is selected as 90 μm.

It can be seen from Eq. (1) that the F-P cavity length value has no effect on the sensitivity. However, the transmission optical length is proportional to the cavity length, and the transmission loss will increase as the optical path length increases. Therefore, the cavity length value of the F-P cavity needs to be as small as possible. It is finally determined that cavity length was 18 μm. Then, the sensitivity of the fiber F-P sensor probe is studied, when d is 2 μm, r is 90 μm and L is 18 μm. Figure 4 shows that the dip of the reflection spectra varies with the pressure, and a polynomial fit curve is given. The simulation reflection spectrum of the fiber F-P sensor is shown in Fig. 4(a). And, a curve fitting of blue shift with pressure is descried in Fig. 4(b), which indicates that the blue shift decreases linearly with the increase of pressure. It can be seen that the sensitivity of this fiber F-P sensor is 1.737 nm/kPa and the linearity can reach 99.99%. Figure 4(c) shows the simulation diagram of the fiber F-P sensor by COMSOL, and Fig. 4(d) shows the finished fiber F-P sensor after packaging.

The detected ultrasonic signal will be demodulated by the intensity demodulation method. The intensity demodulation method uses a linear working interval of the reflection spectra, and converts the cavity length change of the sensor into an intensity

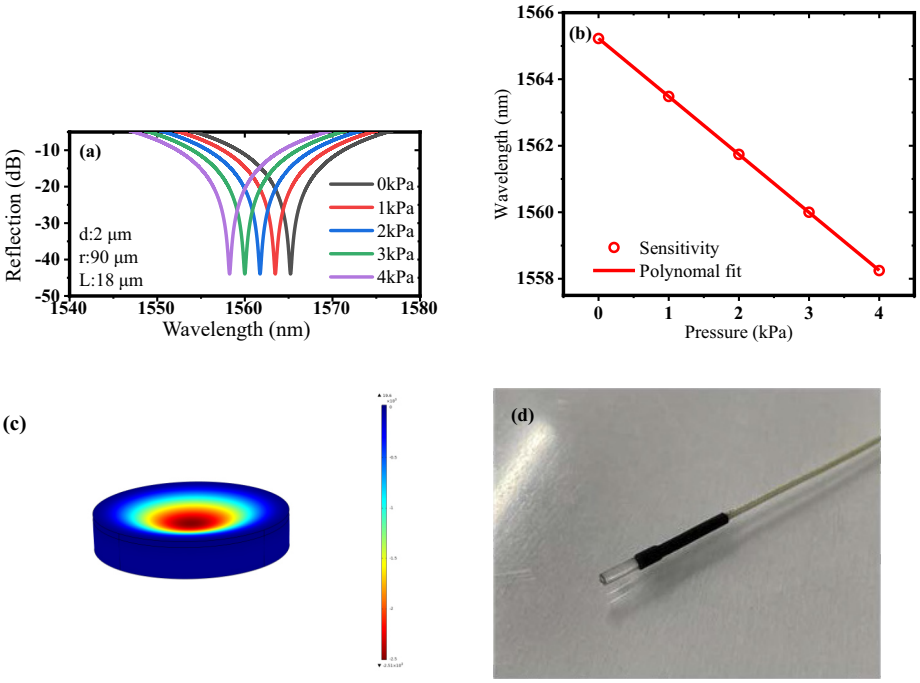

Fig. 4. (a) Reflection spectra of the fiber F-P sensor with d = 2 μm, r = 90 μm and L = 18 μm, (b) the polynomial fits of the wavelength dips, (c) simulation results of diaphragm compression by COMSOL, and (d) the fiber F-P sensor after packaging.

change to realize the demodulation of the F-P ultrasonic sensor signal. Between two wavelength dips of the spectra, there is an obvious linear interval, which is suitable for demodulating F-P ultrasonic sensor signal using intensity demodulation method. As shown in Fig. 5, the monotonic linear interval AB is selected as the working interval of the sensor, and the cavity length value of the sensor can be obtained by measuring the output light power. The demodulation principle can be expressed as

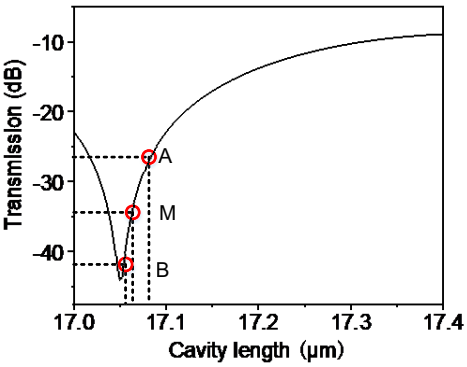

Fig. 5. Schematic diagram of the intensity demodulation method.

$$\begin{cases} L_{\mathrm{M}} = \dfrac{L_{\mathrm{A}} + L_{\mathrm{B}}}{2} \\ I_{\mathrm{M}} = \dfrac{I_{\mathrm{A}} + I_{\mathrm{B}}}{2} \\ k = \dfrac{I_{\mathrm{B}} - I_{\mathrm{A}}}{L_{\mathrm{B}} - L_{\mathrm{A}}} \end{cases} \tag{4}$$

where A, B, M are three points in the linear working range, respectively, and M is the midpoint. L_{A}, L_{B} and L_{M} are the F-P cavity lengths corresponding to the three points A, B, and M, respectively. I_{A}, I_{B} and I_{M} are the intensity of the output light power corresponding to the points A, B, and M, respectively. k is the slop of the line AB.

By measuring the intensity of output light, the cavity length of the sensor can be calculated, then the intensity of the ultrasonic generated by the PD can be obtained. This is the basic principle of the intensity demodulation method of the optical fiber F-P cavity ultrasonic sensor. Its advantages are that the method is direct and simple, the demodulation speed is fast, the response frequency is high and the cost is low. It can be applied to high-frequency signals and weak dynamics.

3. Experiment and analysis

Figure 6(a) shows the schematic of the EFPI ultrasonic sensor system, and Fig. 6(b) depicts the setup of the sensing system. The entire system is divided into a light path part and a circuit part. The system starts data collection by the PC giving instructions to the FPGA high-speed acquisition board (M4i.4450-x8, SPECTRUM-INSTRUMENTATION). At the same time, the narrow linewidth laser source (DL-BF8B-CLS101B -S1550-LW10, DenseLight) emits continuous light and transmits it to the fiber F-P sensor

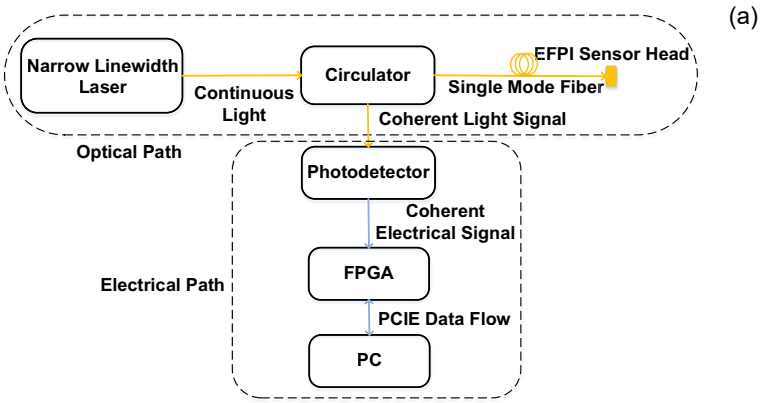

Fig. 6. (a) Schematic of the EFPI ultrasonic sensor system, and (b) structure diagram of the EFPI sensor system.

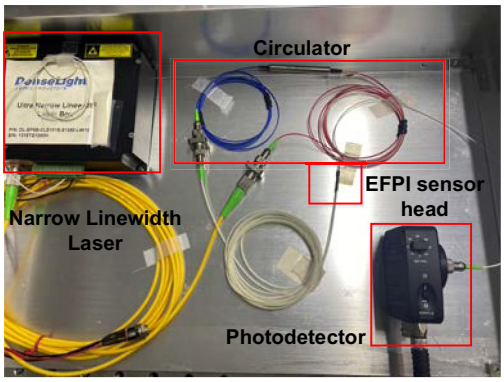

Fig. 6. Continued.

through the circulator. The light will be reflected by the EFPI sensor, then is transmitted to the photodetector (PDA20CS2, THORLABS) module through the circulator. The weak optical signal is converted into electrical signal, and the electrical signal is amplified at photodetector. The electrical signal is output to the PC through the PCIE bus, then the collected data is processed, displayed and saved.

A single frequency acoustic signal is applied to the sensing system for experimental verification. A digital signal generator (RIGOL, DG4102) is used to apply a sinusoidal signal with an amplitude of 10 Vpp and a frequency from 2 kHz to 1.2 MHz to the PZT, which is converted into a sound wave signal to simulate the sonic wave caused by PD. The whole experiment was carried out at 25°C. The fiber F-P sensor is attached to the PZT, and the signal generator is adjusted to a sinusoidal signal of 40 kHz and 1.2 MHz, respectively. The monitored electrical signal output and spectrum are shown

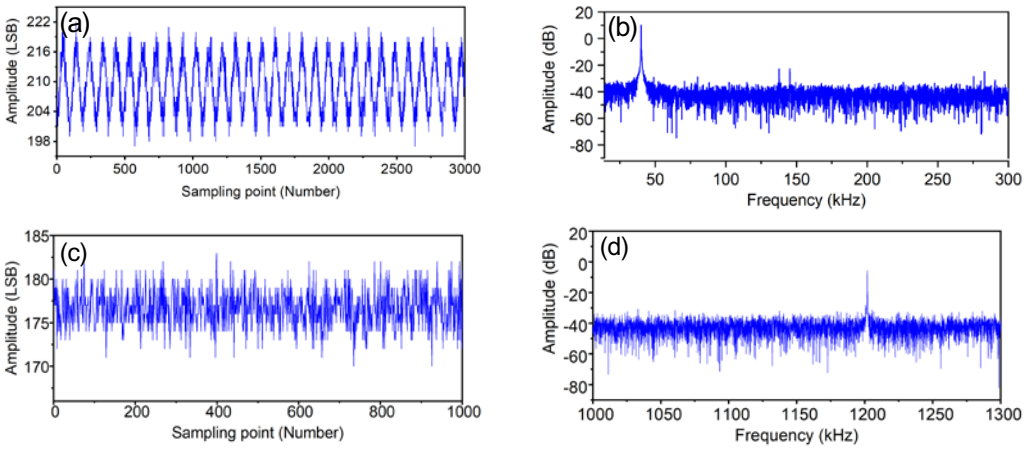

Fig. 7. (a) The output voltage amplitude of the sensor system at 40 kHz, (b) FFT at 40 kHz, (c) the output voltage amplitude of the sensor system at 1.2 MHz, and (d) FFT at 1.2 MHz.

in Fig. 7. As shown in Figs. 7(a) and (b), its spectrum curve rises sharply at the 39 kHz frequency point with an amplitude exceeding 10 dB when a signal with frequency of 40 kHz is applied to the PZT. When the frequency of 1.2 MHz is applied to the PZT, its spectrum curve also rises sharply at the 1.21 MHz frequency point with an amplitude exceeding 10 dB, which is shown in Figs. 7(c) and (d).

More professional experimental verification was carried out in Shanghai Institute of Metrology and Testing to verify the accuracy of the system, the photograph of voltage generator of which is shown in Fig. 8(a). The PD test is carried out with a large voltage of 10 kV. As shown in Fig. 8(b), since the distance between the two electrodes is very close, the air near the two electrodes will generate a great field strength and break down the air, and the discharge is generated, when the power of the voltage generator is turned on. The ultrasonic wave generated by the large voltage can simulate the ultrasonic wave emitted by the PD occurs. The EFPI ultrasonic sensor and PZT are placed at both sides of the electrode to detect the acoustic signal generated when the air is broken down. The PZT is connected to the spectrum analyzer for comparison with the experimental results of the EFPI ultrasonic sensor of this system. The test results of the EFPI ultrasonic sensor are shown in Figs. 9(a) and (b). Because the ultrasonic signal generated by PD is a random signal, many frequency components will be detected, and accordingly many peaks will appear in the spectrum, as shown in Fig. 9(b).

(a)

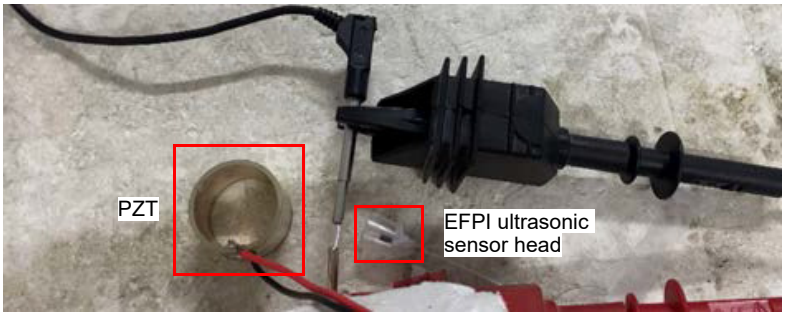

(b)

Fig. 8. (a) The photograph of voltage generator, and (b) the photograph of the test.

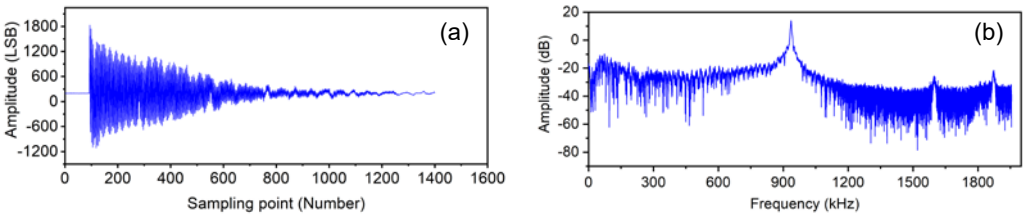

Fig. 9. (a) The output voltage amplitude of the sensor system, and (b) the FFT of output voltage.

A comparison of the EFPI ultrasonic sensor and PZT test results is summarized in Table 1. It demonstrated that the detected frequencies of the EFPI ultrasonic sensor and the PZT are relatively close, but the difference is larger at 1800 kHz, the reason of which is that the signal frequency is higher than the natural frequency of fiber F-P sensor. Hence it will reduce the detection accuracy of EFPI ultrasonic sensor.

T a b l e 1. Detected results comparison of PZT and EFPI ultrasonic sensor.

Frequency detected by PZT (kHz)	75.37	198.14	257.87	486.84	911.59	1160	1389	1800
Frequency detected by EFPI ultrasonic sensor (kHz)	75.86	204.59	250.02	401.29	973.87	1134	1407	1653

Several kinds of EFPI sensors reported are compared in Table 2. It can be clear that the sensor proposed is made of silicon and the size of the sensor is very small. When the sensitivity meets the requirements of ultrasonic signal measurement, the natural frequency of the sensor is much higher than that of the same type of sensor reported in the literature, which can greatly increase the range of sound pressure measurement.

T a b l e 2. Performance comparison of EFPI sensors.

Ref.	Radius	Thickness	Diaphragm materia	Sensitivity	Natural frequency
[28]	900 μm	0.1 μm	Graphene	750 mV/Pa	–
[29]	2300 μm	63 μm	Quartz	0.28 nm/Pa	32.8 kHz
[30]	5000 μm	100 μm	Photosensitive resin material	2.81 mV/Pa	–
[31]	1120 μm	5 μm	Silicon	733 nm/kPa	60 kHz
[32]	2500 μm	200 μm	Quartz	0.012 nm/Pa	88 kHz
[33]	–	–	Silicon	60 nm/kPa	101.5 kHz
This work	90 μm	2 μm	Silica	1.737 nm/kPa	2.1 MHz

4. Conclusion

In this report, an EFPI ultrasonic sensor was designed and investigated. First, the relationship between the sensitivity and the silica diaphragm thickness and the radius of the fiber F-P sensor has been simulated. The frequency of the detected signal must be

less than the natural frequency of the fiber F-P sensor probe. The greater natural frequency, the greater detection range. The sensitivity is 1.737 nm/kPa and theoretical detection range is 2.1 MHz when the silica diaphragm thickness is 2 μm, the silica diaphragm radius is 90 μm, and the cavity length is 18 μm. Second, applying a single frequency acoustic signal with the frequency of 40 kHz and 1.2 MHz to the sensing system, the detected frequency of EFPI ultrasonic sensor was 39 kHz and 1.2 MHz, respectively. The small difference between measurement results and actual values is caused by the inaccuracy of the sensor size and the temperature variation, which indicated that the frequency of this ultrasonic signal can be detected by this EFPI ultrasonic sensor precisely. At last, the more professional experiment has been performed at the Shanghai Institute of Metrology and Testing. The experimental results demonstrated that the ultrasonic signal produced by PD can be detected by EFPI ultrasonic sensor accurately.

Funding
Science and technology project of the State Grid Corporation of China (5600-202021159A-0-0-00).

References

[1] Yu B., Kim D.W., Deng J., Xiao H., Wang A., *Fiber Fabry-Perot sensors for detection of partial discharges in power transformers*, Applied Optics **42**(16), 2003: 3241-3250. https://doi.org/10.1364/AO.42.003241

[2] Chou C.-J., Chen C.-H., *Measurement and analysis of partial discharge of high and medium voltage power equipment*, [In] *Proceedings of the 2018 7th International Symposium on Next Generation Electronics (ISNE)*, 2018: 1-4. https://doi.org/10.1109/ISNE.2018.8394749

[3] Zhou M., Tang Z., *Research on failure identification of partial discharge ultrasonic signal based on GFCC*, [In] *2020 IEEE Electrical Insulation Conference (EIC)*, 2020: 412-416. https://doi.org/10.1109/EIC47619.2020.9158683

[4] Yang N., Gong Y., Bi J., Yang Y., Chang W., *Comparative research on detection effect of partial discharge energized test methods of GIS*, [In] *2018 International Conference on Power System Technology (POWERCON)*, 2018: 3598-3601. https://doi.org/10.1109/POWERCON.2018.8602342

[5] Kelen A., *Trends in PD diagnostics. When new options proliferate, so do old and new problems*, IEEE Transactions on Dielectrics and Electrical Insulation **2**(4), 1995: 529-534. https://doi.org/10.1109/94.407018

[6] Boffi P., Bratovich R., Persia F., Barberis A., Martinelli M., De Maria L., Borghetto J., Perini U., *1550nm all-fiber interferometer for partial discharge detection in oil-insulated power transformer*, [In] *Optical Fiber Sensors*, OSA Technical Digest (CD), Optical Society of America, 2006, paper TuC5. https://doi.org/10.1364/OFS.2006.TuC5

[7] Yum P.S., Campbell F., Eltom A.H., *The diagnostic analysis of partial discharge with acoustic monitoring in GIS equipment*, [In] *IEEE Power Engineering Society Summer Meeting*, Vol. 1, 2002: 196-200. https://doi.org/10.1109/PESS.2002.1043214

[8] Xie X., Mu J., Liu R., Meng Q., Wu S., Lv P., Sun F., Liu B., Zhang B., Zhu B., Zhang F., *Research on partial discharge detection methods for electrical equipment diagnosis*, [In] *Proceedings of the 2016 4th International Conference on Machinery, Materials and Computing Technology*, Atlantis Press, 2016: 1408-1410. https://doi.org/10.2991/icmmct-16.2016.278

[9] Han T., Su J.G., Ma T.T., Wang F.Y., Xing Y.Q., Gao Y., *Partial discharge characteristics during treeing process in silicone rubber at 20 and –100 °C*, IEEE Transactions on Applied Superconductivity **29**(2), 2019: 7700904. https://doi.org/10.1109/TASC.2018.2890516

[10] GAO W., DING D., LIU W., *Research on the typical partial discharge using the UHF detection method for GIS*, IEEE Transactions on Power Delivery **26**(4), 2011: 2621-2629. https://doi.org/10.1109/TPWRD.2011.2166089

[11] SUN S., TIAN L., YU H., SHEN J., *Study of the online monitoring for GIS partial discharge based on UHF method*, [In] *2011 1st International Conference on Electric Power Equipment - Switching Technology*, 2011: 266-270. https://doi.org/10.1109/ICEPE-ST.2011.6122985

[12] UWIRINGIYIMANA J.P., KHAYAM U., *Measurement of partial discharge in air insulation by using UHF double layer bowtie antenna with modified wings edges*, [In] *2019 International Conference on Electrical Engineering and Informatics (ICEEI)*, 2019: 228-233. https://doi.org/10.1109/ICEEI47359.2019.8988866

[13] LI X., LU Q., LI D., CHEN X., LV H., WANG Y., *Transducers arrangement of the UHF-PD online monitoring system for GIS*, High Voltage Apparatus **48**(11), 2012: 70-74.

[14] LI Z., LUO L., SHENG G., LIU Y., JIANG X., *UHF partial discharge localisation method in substation based on dimension-reduced RSSI fingerprint*, IET Generation, Transmission & Distribution **12**(2), 2018: 398-405. https://doi.org/10.1049/iet-gtd.2017.0601

[15] WU X., HAN X., ZHANG L., LI X., MA Y., Li J., *Study on PD detection method in GIS under oscillating impulse voltage based on UHF method*, [In] *2017 1st International Conference on Electrical Materials and Power Equipment (ICEMPE)*, 2017: 305-308. https://doi.org/10.1109/ICEMPE.2017.7982090

[16] OLSZEWSKA A., WITOS F., *Location of partial discharge sources and analysis of signals in chosen power oil transformers by means of acoustic emission method*, Acta Physica Polonica A **122**(5), 2012: 921-926. https://doi.org/10.12693/APhysPolA.122.921

[17] ZHENG Q., MA G., JIANG J., LI C., ZHAN H., *A comparative study on partial discharge ultrasonic detection using fiber Bragg grating sensor and piezoelectric transducer*, [In] *2015 IEEE Conference on Electrical Insulation and Dielectric Phenomena (CEIDP)*, 2015: 282-285. https://doi.org/10.1109/CEIDP.2015.7352071

[18] DONG B., HAN M., SUN L., WANG J., WANG Y., WANG A., *Sulfur hexafluoride-filled extrinsic Fabry –Pérot interferometric fiber-optic sensors for partial discharge detection in transformers*, [In] IEEE Photonics Technology Letters **20**(18), 2008: 1566-1568. https://doi.org/10.1109/LPT.2008.928533

[19] MACIÀ-SANAHUJA C., LAMELA H., GARCÍA-SOUTO J.A., *Fiber optic interferometric sensor for acoustic detection of partial discharges*, Journal of Optical Technology **74**(2), 2007: 122-126. https://doi.org/10.1364/JOT.74.000122

[20] BLACKBURN T.R., PHUNG B.T., JAMES R.E., *Optical fibre sensor for partial discharge detection and location in high-voltage power transformer*, [In] *Sixth International Conference on Dielectric Materials, Measurements and Applications*, 1992: 33-36.

[21] LO Y.L., TSAI T.H., SHIH P.F., *Fiber sensing scanner system based on A-thermal fiber Bragg gratings*, Sensors and Actuators A: Physical **242**, 2016: 32-42. https://doi.org/10.1016/j.sna.2016.02.027

[22] ZHAO Z.Q., MACALPINE M., DEMOKAN M.S., *The directionality of an optical fiber high-frequency acoustic sensor for partial discharge detection and location*, Journal of Lightwave Technology **18**(6), 2000: 795-806. https://doi.org/10.1109/50.848388

[23] MA G., ZHOU H., ZHANG M., LI C., CUI B., WU Y., *Optical fiber acoustic emission sensor for GIS partial discharge detection*, [In] *Optical Sensors and Sensing Congress (ES, FTS, HISE, Sensors)*, OSA Technical Digest, Optica Publishing Group, 2019, paper STh3A.5. https://doi.org/10.1364/SENSORS.2019.STh3A.5

[24] LI H., LV J., LI D., XIONG C., ZHANG Y., YU Y., *MEMS-on-fiber ultrasonic sensor with two resonant frequencies for partial discharges detection*, Optics Express **28**(12), 2020: 18431-18439. https://doi.org/10.1364/OE.391242

[25] YANG Y.J., LEE C.L., *Airgap fiber Fabry-Pérot interferometer using a hollow core fiber coated with a layer of photopolymer for measurement of relative humidity and temperature*, [In] *2016 5th International Symposium on Next-Generation Electronics (ISNE)*, 2016: 1-2. https://doi.org/10.1109/ISNE.2016.7543332

[26] Wang C., Liu X., Peiwen K., Wang P., Zhang L., Chen D., *~1 μm laser output based on heterogeneous fiber with Yb^{3+}-doped fluorophosphate core and phosphate cladding*, Materials Letters **179**, 2016: 9-11. https://doi.org/10.1016/j.matlet.2016.05.033
[27] Di Giovanni M., *Flat and Corrugated Diaphragm Design Handbook*, Marcel Dekker, 1982.
[28] Wu Y., Yu C., Wu F., C. Li, Zhou J., Gong Y., Rao Y., Chen Y., *A highly sensitive fiber-optic microphone based on graphene oxide membrane*, Journal of Lightwave Technology **35**(19), 2017: 4344-4349. https://doi.org/10.1109/JLT.2017.2737639
[29] Pi B., Cao X., Nie D., Cheng L., Jiang X., Liu Y., *Optical fiber F-P partial discharge detection sensor optimization design*, Transformer **55**(5), 2018: 39-43. https://doi.org/10.19487/j.cnki.1001-8425.2018.05.007
[30] Shen S., Wei H., Wang J., Liu H., Ma Z., Chen N., Shang Y., Pang F., *3D printing optical fiber Fabry-Perot cavity acoustic emission sensor*, Chinese Journal of Lasers **47**(9), 2020: 906004. https://doi.org/10.3788/CJL202047.0906004
[31] Huang X., An J., Li J., Wang L., *Optical fiber Fabry-Perot acoustic sensor for partial discharge detection*, Optical Communication Technology, No. 02, 2022: 66-70. https://doi.org/10.13921/j.cnki.issn1002-5561.2022.02.013
[32] Zhao H., Li M., Wang P., Zhang Y., *Non-intrinsic fiber Fabry-Perot sensor for local acoustic measurement in liquid media*, Journal of Electrical Engineering, China, No. 22, 2008: 59-63.
[33] Wang W., Wang Z., Wu Y., Du J., Li F., *Fabry–Perot optical fiber ultrasonic sensing technology for partial discharge detection in oil*, High Voltage Engineering, No. 03, 2014: 814-821. https://doi.org/10.13336/j.1003-6520.hve.2014.03.025

Received May 11, 2022
in revised form August 18, 2022